International Conference on Space Optics—ICSO 2018

Chania, Greece

9–12 October 2018

Edited by Zoran Sodnik, Nikos Karafolas, and Bruno Cugny

Investigation on a SmallSat CMOS image sensor for atmospheric temperature measurement

Jilin Liu

Tom Neubert

Denis Froehlich

Peter Knieling

et al.

esa icso proceedings cnes

International Conference on Space Optics — ICSO 2018, edited by Zoran Sodnik, Nikos Karafolas, Bruno Cugny, Proc. of SPIE Vol. 11180, 111806M · © 2018 ESA and CNES · CCC code: 0277-786X/18/$18 · doi: 10.1117/12.2536157

Investigation on a SmallSat CMOS image sensor for atmospheric temperature measurement

Jilin Liu*[a,b], Tom Neubert[c], Denis Froehlich[c], Peter Knieling[b], Heinz Rongen[c], Friedhelm Olschewski[b], Oliver Wroblowski[a,b], Qiuyu Chen[a,b], Ralf Koppmann[b], Martin Riese[a,b], Martin Kaufmann[a,b]

[a]Institute of Energy and Climate Research (IEK-7), Jülich Research Centre, Germany; [b]Institute for Atmospheric and Environmental Research, University of Wuppertal, Wuppertal, Germany; [c]Central Institute for Engineering, Electronics and Analytics, Electronic System (ZEA-2), Jülich Research Centre, Germany

ABSTRACT

This article presents the characterization and analysis of a commercial off-the-shelf (COTS) CMOS detector utilized in a miniaturized satellite payload for atmospheric temperature measurements. To evaluate the performance of the selected CMOS detector, a series of tests were performed. The temperature dependent dark current, the readout noise and the system gain are determined, which are provided for the subsequent system performance evaluation and data processing. A case study is established to simulate the space radiation effect to determine the needed shielding thickness on the instrument. The effect of radiation damage on the CMOS image sensors is investigated using a Co-60 Gamma radiation source.

Keywords: CMOS, remote sensing, radiation, TID, dark current, readout noise, gain

1. INTRODUCTION

SmallSat missions are playing an increasingly important role in space-based programs. The short development cycles, the low cost and the flexibility make SmallSats a suitable solution for scientific research, instrument concept verification and flight demonstration tasks. Recently, a miniaturized satellite payload[1] based on spatial heterodyne spectrometer (SHS) technology[2-4] is built up for atmospheric temperature measurements. A CMOS imaging detector was selected and integrated to record the interferogram generated by the spectrometer.

The rapid growth of the research and development on CMOS image sensors over last decades offers desirable characteristics for a number of space-based scientific applications, with low power consumption, low cost and high levels of integration compared with conventional CCD detectors[5,6]. The CMOS detector does not suffer from charge transfer degradation from displacement damage since, unlike the CCD, the pixels can be addressed directly. Nevertheless, the CMOS image sensors, especially the commercial off-the-shelf (COTS) parts, currently lack the competitive performance in detector dark current, noise and non-uniformity compared with customized CCD sensors. Therefore, an evaluation on the selected COTS CMOS imager is much needed for a SmallSat payload.

For a space mission the detectors are damaged by cosmic particles or rays, which leads to the performance degradation or even functional failure. Although the radiation hardness technologies of commercial CMOS have been evolving rapidly over the past decades, the performance of typical COTS products is still not guaranteed since this parameter is generally not characterized by the manufacturers[7-9]. Therefore, the radiation test on the COTS CMOS detector is compulsory in the instrument verification period for the space mission. In this study, a Co-60 Gamma radiation source is used to study the effect of radiation damage on the CMOS image sensors.

*j.liu@fz-juelich.de

2. ELECTRONIC AND DETECTOR

The payload readout electronics developed at Central Institute for Engineering, Electronics and Analytics, Electronic Systems (ZEA-2) of Jülich Research Centre (FZJ) consist of two boards: the proximity electronics (PXE) for directly interfacing to the detector ICs and the front-end electronics (FEE) with an embedded controller with ARM cores and FPGA fabric. The FEE serves as the central processing system of the readout system. In addition, a power supply unit (PSU) is integrated to fulfill grounding isolation requirements. The tasks are to handle signals from the control unit (CU) of the satellite bus to start the measurement, to acquire detector data, to provide data pre-processing (data binning) and to transfer data to the CU. A block diagram for the readout electronics is shown in Figure 1.

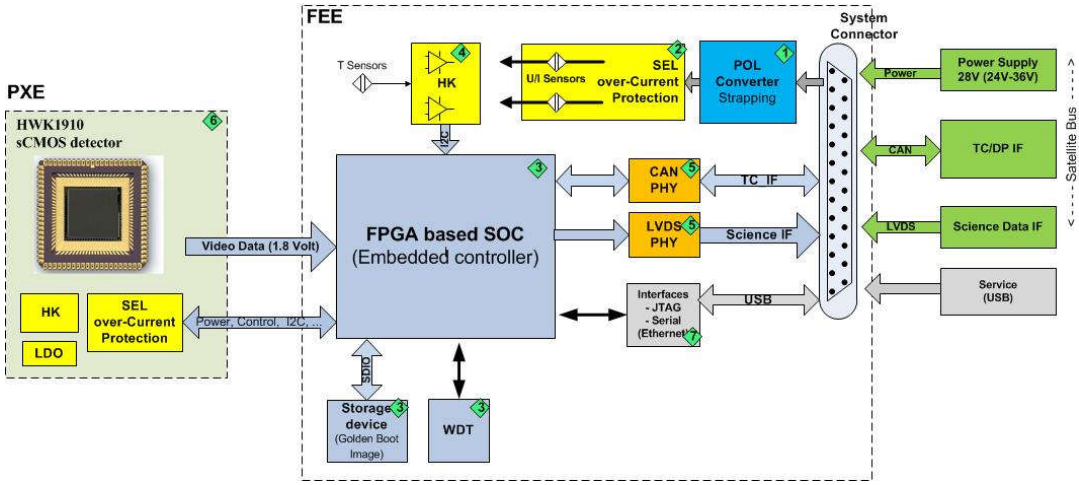

Figure 1. Block diagram of payload readout electronics

A scientific CMOS (sCMOS) imaging detector builds the baseline for the camera system of the experiment. Current sCMOS sensors have a performance competitive with CCD devices. After investigating several vendors for scientific CMOS sensors, a silicon-based CMOS image sensor from Fairchild Imaging (HWK1910A) is chosen for its low noise and high dynamic range. The quantum efficiency at bout 760 nm, which is the wavelength for the measurements, is about 40%. This sensor has common programmable region of interest (ROI) registers, on-chip digitizers (ADCs) and a digital interface to the readout electronics. The pixel size of the detector is 5µm x 5µm, and the ideal number of pixels 1920 x 1080. The detector main specifications are summarized in Table 1.

Table 1. HWK1910A CMOS detector specifications

CMOS	HWK1910A
Pixel count	1920 Horizontal x 1080 Vertical pixels
Pixel size	5.04 microns x 5.04 microns
Active area	9676.8 microns (H) x 5443.2 microns (V)
Read noise	1 electronic (rms)
Dark current	< 20e^-/pixel/s dark current @ 20°C
Gain	0.42e^-/count
Quantum efficiency	40% @ 760nm

Among the different operating modes of the detector, the uncalibrated mode and the manual calibration mode are investigated in this study. The switch between these two operating modes can be realized via sending a telecommand to the instrument during operation. For the manual calibration mode, the sensor goes through an internal offset and column gain calibration cycle to compensate for the different performance of the amplifiers and for temperature drift over time. Figure 2 shows the uncalibrated and calibrated detector test images, where the correction of column gain is clearly visible. The manual calibration mode offers correction of the spatial variation of pixel output.

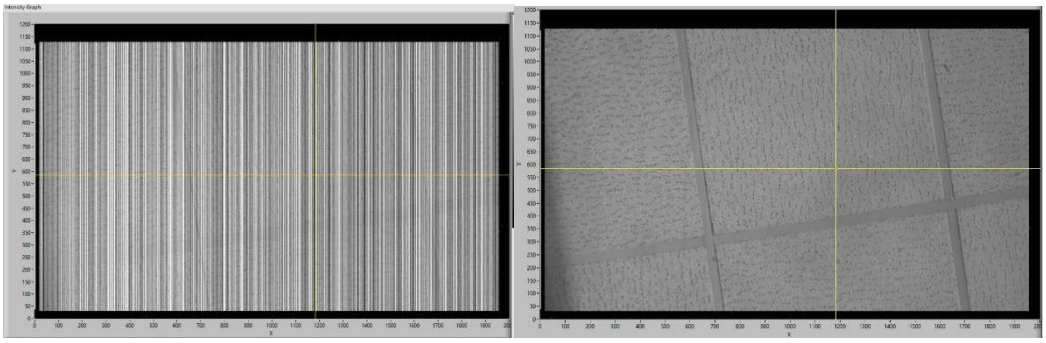

Figure 2. Uncalibrated (left) and calibrated (right) detector test images in the laboratory

3. DETECTOR PERFORMANCE TESTS

Detector dark currents

The HWK1910A device was tested in a thermal chamber to characterize the temperature dependence of the detector dark current with various integration times. Several temperature sensors were set inside the chamber and on the detector to monitor the detector and environmental temperatures. During the test, the detector dark current was measured between -15°C and +25°C.

Figure 3 displays the dark current profile as an ensemble average of the entire array at different temperatures. For these measurements, the detector bias was measured with the shortest integration time and subtracted for each dark frame. The dark current at 20°C is about 2.5 e^-/s/pixel, which is a factor of 8 lower than the threshold provided by the manufacturer. Based on the linear integration time dependency and the exponential temperature dependency of the detector dark current, a model was established to predict the detector dark current for each pixel, as shown in the red curve for averaged results on the detector array. According to the fitted parameters, the detector dark current doubles for every 6.4 K *temperature* change.

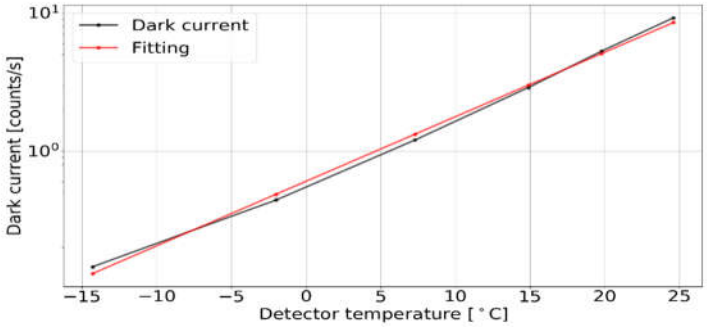

Figure 3. Temperature dependency of the detector dark current between −15°C and +25°C. The black line represents the measurement, and the red line corresponds to the result from model estimation.

System gain and readout noise

The detector system gain usually describes to the conversion ratio from the number of electrons into Analog-Digital Units (ADUs). This parameter can be estimated from the shot noise characteristic associated with the signal intensity, namely the mean-variance method (MVM) or the photon transfer curve[10,11]. The Poisson distribution of the shot noise gives the shot noise variance σ_{shot}^2 which is equal to the averaged signal intensity S in ADUs. The total noise variance σ_{noise}^2 can therefore be expressed as:

$$\sigma_{noise}^2 = G^2 \sigma_{shot}^2 + \sigma_{readout}^2 = G\,S + \sigma_{readout}^2 \quad (1)$$

where G is the system gain in ADUs/electron and $\sigma_{readout}^2$ represents the readout noise variance which has zero mean. Accordingly, the linear fit of the total noise variance against the averaged signal intensity S gives the conversion gain G and the offset that corresponds to the readout noise variance.

For this measurement a light source was installed inside the thermal chamber. The detector temperature was cooled down below −20°C to minimize the detector dark current. The amount of photons recorded by the detector was controlled by adjusting the integration time. From the linear regression analysis the distribution of the estimated system gain under different integration times was obtained (Figure 4). This estimation indicates that the average conversion ratio is about 2 ADUs/electron and the corresponding readout noise is about 1e^-, which are close to the detector specifications provided by the manufacturer.

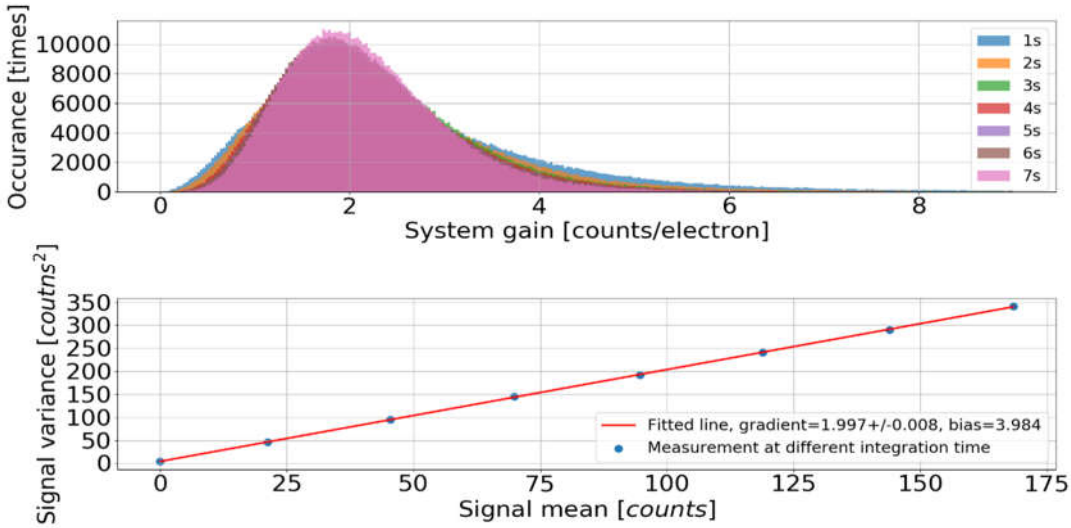

Figure 4. Estimation of system gain

Another method to characterize the detector readout noise is to determine the standard deviation of various read-outs at zero integration time (Figure 5). This method does not require a light source. For the detector analyzed in this study, the median value is approximately 0.9e^- on each pixel, which fits to the results from MVM method. The corresponding root mean square (rms) is 3.9e^-, which is slightly higher than the given information.

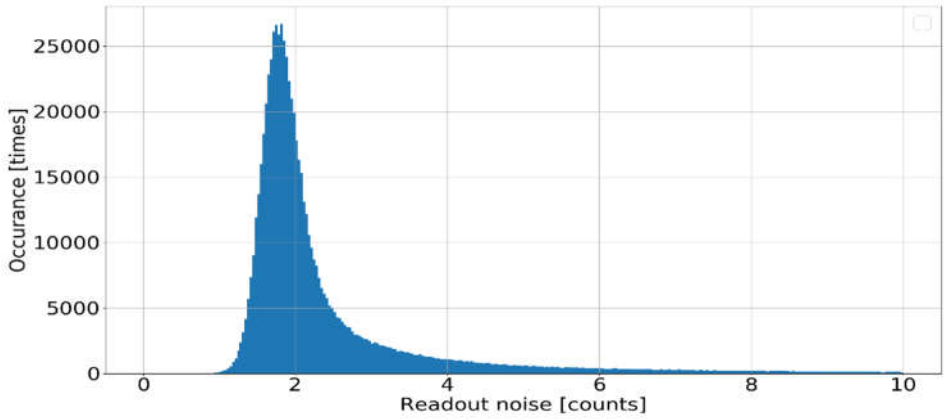

Figure 5. Detector readout noise

System gain and readout noise

The detector fixed pattern noise (FPN) describes a spatial variation in pixel outputs of an image under uniform illumination conditions. For CMOS detectors that use column amplifiers configuration, the FPN appears as "stripes" on the readout images. The manual calibration mode of the detector allows the correction of this pixel gain variation on the whole detector plane, as shown in Figure 2. This operation is achieved by injecting electrons into detector pixels specifically reserved for this calibration purpose. This calibration mode will change the pixel offsets slightly in each power loop, since this procedure is also bound up with the environmental conditions.

The investigation of the pixel offset variation, which is also called the detector fixed pattern, is achieved by running several power loops. The detector integration time was set to be 1ms such that the dark current is negligible for the analysis. During each loop, frames were recorded every 5 s. As illustrated in Figure 6(a), the fixed pattern in loop 1-4 changes slightly, meanwhile the result from the 5th loop shows relative larger deviation than the first 4 loops, which is possibly associated with the environmental temperature at that time. For the instrument radiometric calibration, the detector pixel offsets need to be measured and subtracted each time when the instrument is switched on, simply by taking images at lowest integration time.

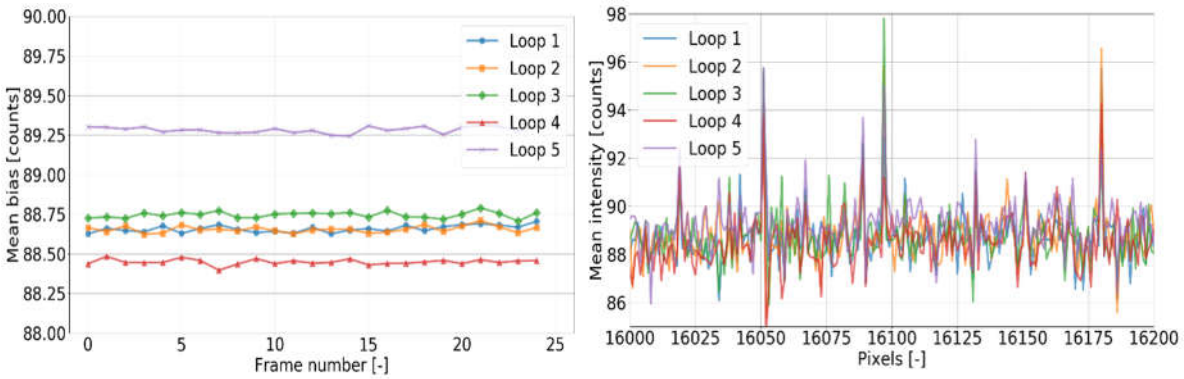

Figure 6. Left (a): detector mean fixed pattern at shortest integration time from 5 power loops. Right (b): detector fixed pattern at certain detector region. Loop 1-4 were measured with 3 minutes in between, while the 5th loop was measured 0.5h after the 4th loop.

4. RADIATION TEST

Radiation environment modelling

The ionizing effect in the space radiation environment can cause degradation and failure of electronic devices, especially when using optoelectronic detectors. Basically the radiation effects consist of two parts: the single event effect (SEE) and the total ionizing dose (TID). The SEE induced by high energy particles will result in device logic failure as an instantaneous failure mechanism, whereas the TID will make cumulative long term ionizing damage on the detectors for low earth orbit (LEO) mission due to protons and electrons exposure. These particles and rays create shifts in threshold voltages and leakage currents, therefore causing permanent radiation damage to Silicon devices.

The increase of dark current is one of the most critical effects on the detector degradation in space radiation environments. The growth of the CMOS dark current under radiation is mainly caused by the generated interface traps and bulk defects, producing additional surface leakage current and bulk current. The ionizing energy transfer generally leads to an increase of the detector dark currents, whereas the non-ionizing mechanism results in the displacement damage dose (DDD) effect, increasing the dark signal non uniformity (DSNU)[12,13].

The commercial and industrial components generally do not provide radiation tolerance performance, therefore those devices need to be tested under expected space environmental radiation. The TID accumulated during satellite missions depends on the orbit, the mission duration and the shielding. TID effects can be reduced using radiation hardened devices and shielding.

To estimate the reliability of the COTS parts used in our experiment and to determine the required thickness of a radiation shield, the TID was calculated depending on the shielding thickness and different mission scenarios using the SPENVIS tool provided by ESA[14]. For this estimation, a satellite flying in a sun-synchronous orbit at an altitude of 1000 km is assumed. Mission durations are 3 years and 5 years, respectively. As a worst case scenario, models for the trapped proton and electron fluxes were the Proton model AP-8 at solar minimum and the Electron model AE-8 at solar maximum[15].

Figure 7 illustrates the SPENVIS output for the accumulated radiation dose for a mission lifetime of 5 years with different Aluminum layer thicknesses. The SHIELDOSE-2 is selected for the ionizing dose model, and the shielding is considered as center of Al spheres[14]. The trapped electrons, as the dominate source of the TID, are largely reduced by increasing the thickness of the medium, since the electrons have a low penetration depth and are therefore easy to shield. Meanwhile, the decrease of trapped protons are not pronounced.

The TID reaching the electronics becomes inefficiently reduced for aluminum thickness greater than 4 mm. The TID for 3 year and 5 year missions with 3mm shielding are 11.4 krads and 19.4 krads, these values reduce to 2.4 krads and 4.1 krads when the semi-infinite aluminum medium model is defined for the shielding. Therefore, to guarantee a nominal lifetime of 3 years the instrument should be able to survive under 11.4 krads radiation without considering the shielding of the satellite.

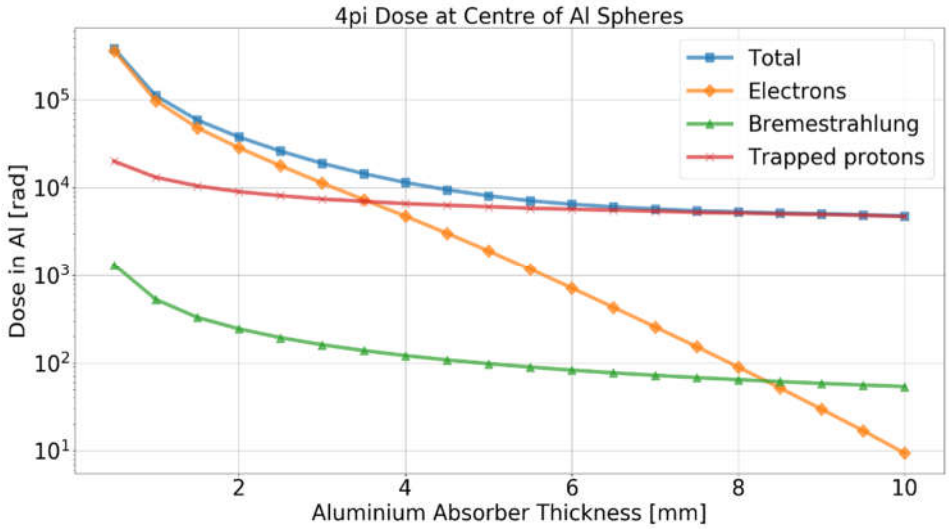

Figure 7. Effective dose vs. aluminum shielding thickness for a 5 years mission from SPENVIS. A sun-synchronous orbit at an altitude of 1000km is assumed.

Radiation test

During the radiation test, the readout electronics in the instrument were classified in modules, which were irradiated in separate steps with different total doses. Radiation tests were made to assure the functionality of the electronics and the detector for the designed mission lifetime. These tests were performed at the Fraunhofer Institute for Technological Trend Analysis (INT), where the samples were irradiated with Co-60 gamma radiation. The actual received radiation was calculated based on the distance to the radiation source. In this paper we mainly focus on the radiation effect on the detector.

Figure 8 shows a photograph taken for the experiment of the radiation test on the CMOS detector. To guarantee the full functionality of the electronics during the detector test, lead blocks were used to protect the remaining parts of the printed circuit board (PCB). The detector was irradiated up to 30 krads under uncalibrated mode, the manual calibration mode was activated from then on. The standalone test of the detector indicates that the detector component worked normally until accumulating 85.25 krads radiation, then all detector pixels became saturated.

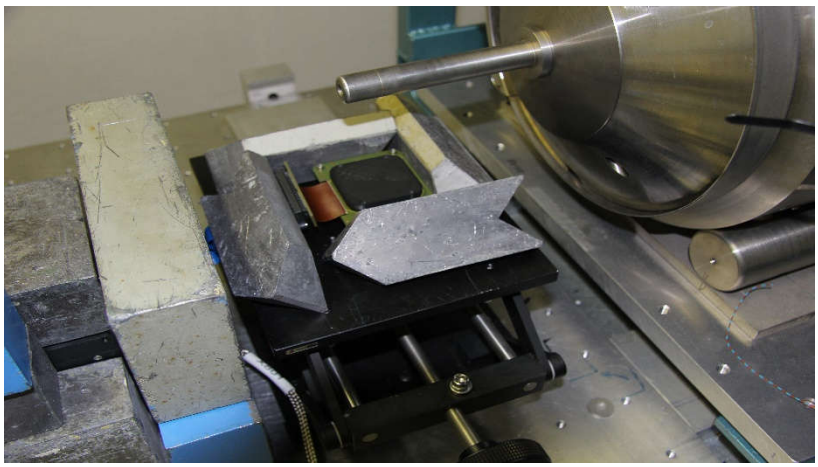

Figure 8. Radiation test on the detector board, the lead blocks were used to shield other electronics.

The detector was set to record images continuously during the radiation test. Dark current measurements were taken when the radiation source was switched off. Figure 9 illustrates the dark images measured at two different radiation doses. Since the manual calibration mode was switched on after 30 krads irradiation on the detector, the dark current at 30 krads is

already quite remarkable. Nevertheless, the detector dark current increases with the increasing radiation dose. In contrast, the "hot pixels" were not significant since the Co-60 gamma radiation generally causes less DDD effect. Figure 10 shows two dark current histograms of the detector for the radiation test, where the long tail of the distribution after radiation is clearly shown. The dark signal after radiation shows a remarkable increase, where the corresponding rms changes from 1538 counts to 3247 counts.

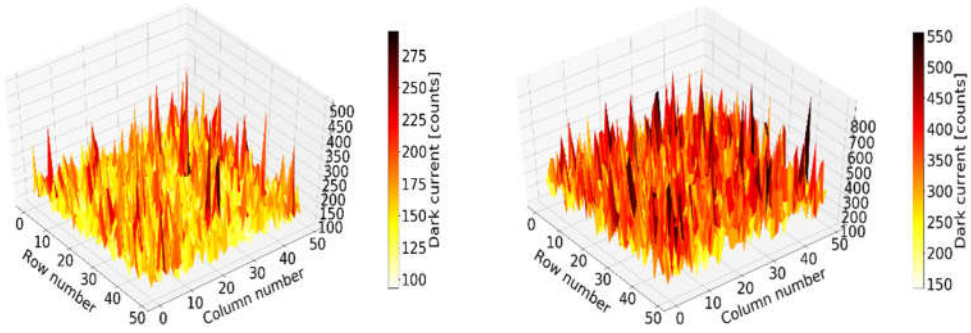

Figure 9. 3-D intensity plots of pixel dark current measured at two different radiation doses for 50 x 50 pixels, detector operated under manual calibration mode with integration time 100ms. Left: radiation dose for 30 krads, right: radiation dose for 60 krads.

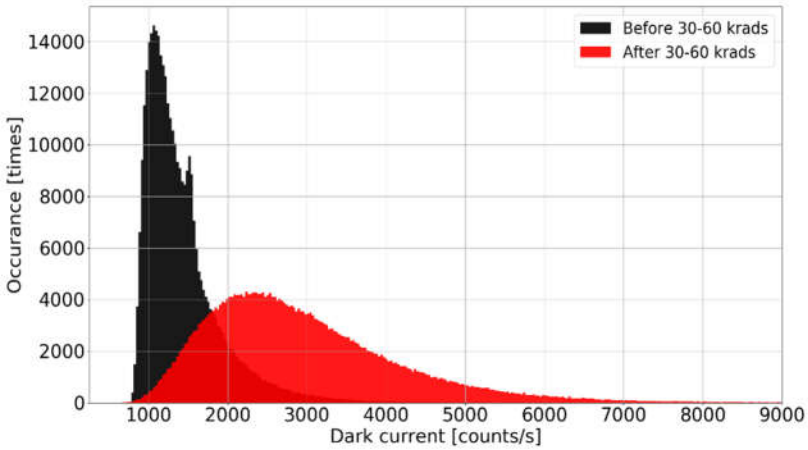

Figure 10. Dark current histograms of the detector measured under manual calibration mode, an image area of 600 rows and 600 columns is chosen.

5. CONCLUSION

In this paper, we described the study of a COTS CMOS image sensor used on a SmallSat payload for atmospheric temperature measurements. Characterization of the detector dark current, readout noise, gain and offset shows that the detector parameters meet the product description provided by the manufacturer. A case study is shown for the estimation of space radiation effect on the instrument. Along with the developed detector readout board, the detector chip has been qualified up to 85 krads radiation. The results presented confirm that the detector system fulfills the requirement of a three to five years low earth orbit mission.

REFERENCES

[1] Kaufmann M, Olschewski F, Mantel K, et al. A highly miniaturized satellite payload based on a spatial heterodyne spectrometer for atmospheric temperature measurements in the mesosphere and lower thermosphere. Atmospheric Measurement Techniques, 2018, 11(7): 3861-3870.
[2] Harlander J M, Roesler F L. Spatial heterodyne spectroscopy: a novel interferometric technique for ground-based and space astronomy//Instrumentation in Astronomy VII. International Society for Optics and Photonics, 1990, 1235: 622-634.
[3] Watchorn S, Roesler F L, Harlander J M, et al. Development of the spatial heterodyne spectrometer for VUV remote sensing of the interstellar medium//UV/EUV and Visible Space Instrumentation for Astronomy and Solar Physics. International Society for Optics and Photonics, 2001, 4498: 284-296.
[4] Roesler, F. L.: An Overview of the SHS Technique and Applications, in: Fourier Transform Spectroscopy/ Hyperspectral Imaging and Sounding of the Environment, Optical Society of America, https://doi.org/10.1364/FTS.2007.FTuC1, 2007
[5] Magnan P. Detection of visible photons in CCD and CMOS: A comparative view. Nuclear Instruments and Methods in Physics Research Section A: Accelerators, Spectrometers, Detectors and Associated Equipment, 2003, 504(1-3): 199-212.
[6] Holst G C. CMOS/CCD sensors and camera systems. " CMOS/CCD sensors and camera systems/Gerald C. Holst, Terrence S. Lomheim. Published:, 2007.
[7] Lacoe R C, Osborn J V, Mayer D C, et al. Total-dose radiation tolerance of a commercial 0.35/spl mu/m CMOS process//Radiation Effects Data Workshop, 1998. IEEE. IEEE, 1998: 104-110.
[8] Faccio F. COTS for the LHC radiation environmentain: the rules of the game. 2000.
[9] Felix J A, Dodd P E, Shaneyfelt M R, et al. Radiation response and variability of advanced commercial foundry technologies. IEEE transactions on nuclear science, 2006, 53(6): 3187-3194.
[10] Beecken B P, Fossum E R. Determination of the conversion gain and the accuracy of its measurement for detector elements and arrays. Applied optics, 1996, 35(19): 3471-3477.
[11] Stark B, Noelting B, Jahn H, et al. Method for determining the electron number in charge-coupled measurement devices. Optical Engineering, 1992, 31(4): 852-857.
[12] Srour J R, Hartmann R A, Kitazaki K S. Permanent damage produced by single proton interactions in silicon devices. IEEE Transactions on Nuclear Science, 1986, 33(6): 1597-1604.
[13] Hall G. Radiation damage to silicon detectors. Nuclear Instruments and Methods in Physics Research Section A: Accelerators, Spectrometers, Detectors and Associated Equipment, 1995, 368(1): 199-204.
[14] Heynderickx, D., et al. "ESA's Space Environment Information System (SPENVIS)-A WWW interface to models of the space environment and its effects." *38th Aerospace Sciences Meeting and Exhibit*. 2000.
[15] Heynderickx, D., et al. "Calculating low-altitude trapped particle fluxes with the NASA models AP-8 and AE-8." *Radiation measurements* 26.6 (1996): 947-952.